Earth-mass haloes and the emergence of NFW density profiles

Raul E. Angulo,[1][*] Oliver Hahn,[2] Aaron D. Ludlow[3] and Silvia Bonoli[1]

[1] *Centro de Estudios de Física del Cosmos de Aragón (CEFCA), Plaza San Juan 1, Planta-2, Teruel, E-44001, Spain*
[2] *Laboratoire Lagrange, Université Côte d'Azur, Observatoire de la Côte d'Azur, CNRS, Blvd de l'Observatoire, CS 34229, F-06304 Nice cedex 4, France*
[3] *Department of Physics, Institute for Computational Cosmology, University of Durham, South Road, Durham DH1 3LE, UK*

ABSTRACT

We simulate neutralino dark matter (χDM) haloes from their initial collapse, at $\sim$ earth mass, up to a few percent solar. Our results confirm that the density profiles of the first haloes are described by a $\sim r^{-1.5}$ power law. As haloes grow in mass, their density profiles evolve significantly. In the central regions, they become shallower and reach on average $\sim r^{-1}$, the asymptotic form of an NFW profile. Using non-cosmological controlled simulations, we observe that temporal variations in the gravitational potential caused by major mergers lead to a shallowing of the inner profile. This transformation is more significant for shallower initial profiles and for a higher number of merging systems. Depending on the merger details, the resulting profiles can be shallower or steeper than NFW in their inner regions. Interestingly, mergers have a much weaker effect when the profile is given by a broken power law with an inner slope of -1 (such as NFW or Hernquist profiles). This offers an explanation for the emergence of NFW-like profiles: after their initial collapse, $r^{-1.5}$ χDM haloes suffer copious major mergers, which progressively shallows the profile. Once an NFW-like profile is established, subsequent merging does not change the profile anymore. This suggests that halo profiles are not universal but rather a combination of (1) the physics of the formation of the microhaloes and (2) their early merger history – both set by the properties of the dark matter particle – as well as (3) the resilience of NFW-like profiles to perturbations.

Key words: large-scale structure of Universe – cosmology: theory.

1 INTRODUCTION

Soon after the first *N*-body simulations reached sufficient mass and force resolution, they revealed that the spherically averaged density profiles of cold dark matter (CDM) haloes have a central density cusp with a sharp decline towards their outskirts (e.g. Frenk et al. 1988; Dubinski & Carlberg 1991; Gelb & Bertschinger 1994). Overall, the density profiles appeared to be well described by a very simple functional form,

$$\rho(x) \propto \frac{1}{x} \frac{1}{(1+x)^2}, \qquad (1)$$

(Navarro, Frenk & White 1996, 1997, hereafter the NFW profile) regardless of halo mass, cosmological parameters or the details of the fluctuation power spectrum (e.g. Cole & Lacey 1996; Huss, Jain & Steinmetz 1999; Bullock et al. 2001; Wang & White 2007; Lovell et al. 2012). Even today, after decades of advances in computational power and techniques – with improvements of over a factor of 10^5 in particle number and 10^2 in force resolution (Diemand,

Kuhlen & Madau 2007; Springel et al. 2008; Gao et al. 2012) – the universality and the asymptotic slope of the density profile of ~ -1 still holds with only minor corrections (e.g. Navarro et al. 2010). This is arguably one of the most important results in computational cosmology to date, yet it is puzzling when contrasted with the expectations of early analytic treatments of the cold collapse of primordial fluctuations (Gunn & Gott 1972; Fillmore & Goldreich 1984; Bertschinger 1985). In particular, these models predict simple power-law density profiles whose slope depends sensitively on that of the initial collapsing patch.

Although the origin of the NFW shape and its universality are still under debate there has been no lack of attempts to explain it. For example, Ludlow et al. (2013) argued that, when expressed in appropriate units, the NFW profile is indistinguishable from that of the scale-free shape of CDM halo mass accretion histories. In this interpretation, the NFW profile simply reflects the typical background density dependence of mass accretion on to growing dark matter (DM) haloes. Other authors apply principles of maximum entropy or adiabatic invariance to show how profiles similar to equation (1) may result from strong mixing associated with mergers and accretion occurring during halo assembly (e.g. Taylor & Navarro 2001; Dalal, Lithwick & Kuhlen 2010; Pontzen &

Governato [2013]; Juan et al. [2014]), or highlight the importance of angular momentum in driving profiles towards the NFW shape (e.g. Lentz, Quinn & Rosenberg [2016]). Others speculate whether the graininess of the *N*-body method might spuriously drive the profiles to the NFW shape (e.g. Baushev [2015]).

Simulations that resolve the free-streaming scale of the DM particle may shed light on the physical origin of DM halo density profiles. The free-streaming scale is the only relevant scale in DM cosmologies: it initiates a well-defined and finite hierarchy of structure and implies that the first haloes can be numerically resolved given adequate resolution. This is quite different from the 'standard' CDM simulations (i.e. in the perfectly cold limit), where DM traces perturbations to arbitrarily small scales such that there are always density perturbations in the DM at the resolution limit. In this case, the first haloes are resolved with just a few particles and thus can be heavily influenced by numerical noise that is arguably at least of comparable magnitude as the physical perturbations on mean interparticle scales.

For the lightest neutralino in supersymmetric extensions to the standard model of particle physics, which should have a mass close to 100 GeV, the free-streaming scale corresponds to about an earth mass (Hofmann, Schwarz & Stöcker [2001]; Green, Hofmann & Schwarz [2004]; Diemand, Moore & Stadel [2005]). While it is computationally impossible given today's resources to simulate the full hierarchy of DM haloes from microhalo to galactic scales, it *is* possible to simulate the formation of the first haloes by focusing on high redshifts and small volumes (e.g. Diemand et al. [2005]). Such simulations have had a rather unexpected outcome: the density profiles of microhaloes appear to deviate substantially from the NFW shape. Instead, they are better described by a single, steep power law, $\rho \propto r^{-1.5}$ (Diemand, Moore & Stadel [2005]; Ishiyama, Makino & Ebisuzaki [2010]; Anderhalden & Diemand [2013]). This appears to be a stable configuration and not simply a transient product of a rapid mass accretion (see Ishiyama [2014]). In addition, Ishiyama ([2014]) found that the average profiles of haloes approach the NFW form as their masses grow well above the free-streaming scale. Conversely, for a perfectly cold CDM spectrum without a cut-off, haloes *always* exhibit an NFW profile, regardless of their mass.

Clearly, the discussion above raises several important questions: What is the physics that determines the density profiles of the first generation of DM haloes? Why do single power laws describe well some haloes, while others are better described by gently curving profiles, such as the NFW form? What is the mechanism that transforms the initial power-law profiles of neutralino haloes to NFW-like profiles at later times? What is the role of their assembly history in establishing the initial profile shape and in its subsequent evolution? Are (at least) some of these results driven by numerical noise and convergence problems of the *N*-body method? All these questions need to be answered to obtain a complete picture of the physics behind the equilibrium (or, at least, stable) state of collapsed objects in the Universe.

In this paper, we directly address some of these issues using zoom simulations of six neutralino-DM (χDM) haloes, which we follow from their first collapse at the free-streaming scale until they have reached $\sim$0.02 M$_\odot$. We show that haloes initially have power-law profiles, $\rho \propto r^{-1.5}$, a form which is preserved during periods of smooth accretion. However, we find that our haloes undergo a transformation in which their density profiles move towards a broken power-law form. We investigate a possible origin of this transformation using a suite of idealized, non-cosmological merger simulations. We find clear evidence that a

flattening of the central slope is a natural outcome of a fluctuating potential produced by mergers. However, these simulations also show that the final profile depends strongly on the number as well as on the initial profiles of the merging systems. In particular, NFW-like profiles appear significantly more stable to such strong perturbations than simple power laws. Although there are still open questions, these results offer useful insights into the physical processes relevant for the emergence of universal density profiles.

The outline of this article is as follows. First, in Section 2, we describe our cosmological simulations of χDM haloes and the main aspects of our analysis, followed by a discussion of the density profiles of these objects in Section 2.3. In the second part, we focus on non-cosmological simulations. In Section 3, we detail the methods employed for generating different equal-mass merger configurations and then discuss the simulation results, focusing mainly on the transformation of density profiles due to temporal oscillations of the central potentials. Finally, in Section 4 we discuss and interpret our aresults in a broader context and provide a concluding discussion.

2 NUMERICAL SIMULATIONS

We use cosmological simulations to study the formation histories and internal structure of the first haloes to collapse in a universe dominated by χDM. All of our runs adopt the following cosmological parameters: $\Omega_m = 0.3$, $\Omega_\Lambda = 0.7$, $h = 0.7$, $n_s = 1$ and $\sigma_8 = 0.87$. Here, Ω_i refers to the current energy density of component *i* in units of the critical density, ρ_{crit}; *h* is the Hubble parameter, expressed in units of 100 km s^{-1} Mpc; n_s is the spectral index of primordial density perturbations and σ_8 is the rms density fluctuation measured in 8 Mpc spheres, linearly extrapolated to $z = 0$. We adopt a transfer function consistent with a standard neutralino particle of mass $m_\chi = 100$ GeV, with a decoupling temperature of $T = 33$ MeV (see e.g. Green et al. [2004]), which we have implemented in the publicly available MUSIC code (Hahn & Abel [2011]). The resulting linear theory power spectrum is shown in Fig. [1] using a solid line.

In such a cosmology, the free streaming of neutralino particles in the early Universe suppresses the growth of density perturbations below a characteristic scale of $\sim$0.7 pc. This implies that the very first objects to collapse (which are also the most abundant) do so at $z > 60$ and have masses of order 10^{-6} M$_\odot$ (Green et al. [2004]; Diemand et al. [2005]; Angulo & White [2010]). Due to the enormous dynamic range required, it has not yet been possible to carry out self-consistent *N*-body simulations that follow the full hierarchical growth of DM haloes from the free-streaming mass up to galactic scales. Furthermore, the need to also properly model large-scale modes in a DM model has hampered efforts to simulate neutralino haloes of the lowest mass from their formation epoch to the present day. For that reason, their internal structure and spatial distribution within the haloes of galaxies like the Milky Way has not yet been properly characterized.

Here, we will perform a simulation of a relatively large region at high redshift and use this run to identify and excise objects for re-simulation at much higher resolution. Doing so will allow us to resolve the initial collapse at the free-streaming scale, and to follow in detail the subsequent evolution of these haloes as they grow in mass by several orders of magnitude. In the following subsections, we summarize the relevant details of these simulations.
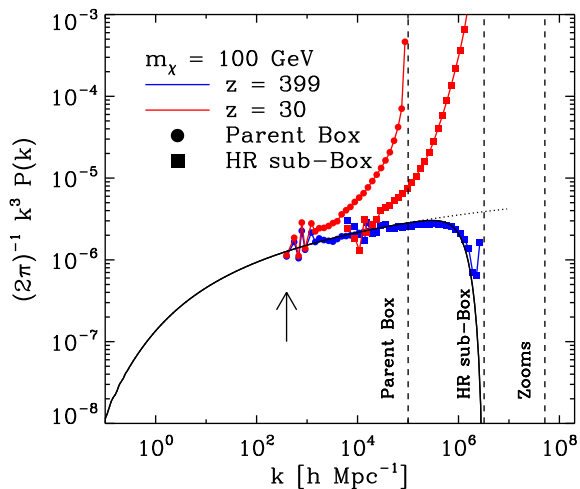
Figure 1. The linear power spectrum of mass fluctuations assuming DM to be composed of neutralinos of mass $m_\chi = 100$ GeV. The solid line corresponds to the linear theory power spectrum employed to set up our simulations; the dotted line shows, for comparison, the power spectrum of a CDM model without a small-scale cut-off. Red and blue symbols indicate the power spectra measured in our parent simulation at $z = 30$ and $z = 399$, respectively, both linearly scaled to $z = 0$. In both cases, circles indicate the spectra of the whole $16\ h^{-1}$ kpc parent box, whereas squares that of the central $1\ h^{-1}$ kpc box followed at higher resolution. The vertical arrow shows the fundamental mode of our simulations, and the vertical dashed lines mark the particle Nyquist frequency for the whole parent box, high-resolution subbox and for the zoom simulations.

2.1 Numerical set-up

2.1.1 The parent simulation

Initial conditions for our parent simulation use 512^3 particles of mass $7.4 \times 10^{-7}\ \mathrm{M}_\odot$ to sample the linear density field within a cubic region of side-length $L = 1.4$ kpc, which is itself embedded into a larger, lower resolution, periodic box of $L = 22.85$ kpc. Particle positions and velocities are generated using second-order Lagrangian perturbation theory at a starting redshift of $z = 399$, which is sufficiently high to ensure that perturbations on the smallest resolved scales are well within the linear regime. Gravitational evolution was simulated using a Tree+PM algorithm implemented in the P-GADGET3 code (Springel et al. 2008), down to a final redshift of $z = 30$ and using a softening length parameter $\epsilon = 0.1$ pc.

The power spectrum measured at the starting redshift is shown in Fig. 1 using blue symbols, which agrees well with the linear theory prediction. Note the characteristic suppression of fluctuations on scales $k \gtrsim 10^6\ h^{-1}\ \mathrm{Mpc}^{-1}$. On these scales the logarithmic slope of the power spectrum is close to -3, and fluctuations on a broad range of spatial scales are expected to collapse simultaneously (this is due to a similar amplitude of the mass variance on those scales). Halo growth is therefore initially very rapid and, shortly after the first objects collapse, the non-linear scale approaches the size of the box. As a result, large boxes are required to properly simulate the evolution of the first χDM haloes. In our case, the parent box-length is $\sim$3000 times larger than the virial radius of the least massive target halo. As we can see from a comparison of the initial (blue symbols) and final (red symbols) power spectra, only the four lowest modes are still well described by linear theory. Thus, by the final output, the non-linear scale is comparable to (but still smaller than) the box size. We note, however, that missing large-scale modes plausibly affect the time of collapse of our haloes to some degree;

boxes of several cubic Mpcs or larger are required to achieve full convergence (Ishiyama et al. 2010). Nevertheless, the formation and evolution of haloes will be qualitatively correct: the gravitational collapse of a cold fluid with a given initial density spectrum, followed by multiple mergers and smooth mass accretion. Note also the offset between the spectra of the parent box (circles) and that of the high-resolution subbox (squares), which is caused by the latter being a relatively underdense region.

The above considerations can be visually appreciated in Fig. 2, which shows the density field at the final output of our simulation. Clearly visible are very extended regions where fluctuations have not yet fully collapsed. These give rise to an incipient network of filaments and only a handful of highly clustered haloes (corresponding to the rarest peaks in the simulation volume) can be clearly identified (indeed, at this redshift only 0.7 per cent of the mass is associated with *any* halo). The surroundings of this region are also overdense, which emphasizes the fact that multiple scales reach the threshold for collapse at similar times.

2.1.2 The re-simulation suite

At the $z = 30$ output time, we identified haloes in the high-resolution parent subbox using an FoF algorithm (Davis et al. 1985) with a linking length $l = 0.2$, and selected for re-simulation the six most massive objects, regardless of their properties. These haloes have virial masses of the order of $10^{-2}\ \mathrm{M}_\odot$, and are resolved with between 10^4 and 2×10^4 particles. Next, we selected a spherical region of radius $2 \times R_{\mathrm{vir}}$ [1] surrounding each halo and tracked the positions of all enclosed particles back to the unperturbed lattice. We then used MUSIC to identify the convex hull containing these particles and to resample this region at higher resolution. Our re-simulations adopt a high-resolution particle mass of $m_p = 2.163 \times 10^{-10}\ \mathrm{M}_\odot$, which is equivalent to having sampled the full simulation volume with $131\,072^3$ particles. Such high resolution allows us to resolve the first non-linear objects (with masses $3 \times 10^{-6}\ \mathrm{M}_\odot$) with roughly 10^4 particles, and the final haloes with $\sim$10^8 particles.

As for our parent run, the gravitational evolution was simulated using the P-GADGET3 code, with forces computed using a Tree+PM algorithm. We employ two particle meshes: one periodic mesh covering the whole simulation volume, and a non-periodic one covering only the location of high-resolution region. Our runs adopt a Plummer-equivalent softening length equal to $\epsilon = 0.002$ comoving pc (approximately 4000 times smaller than the virial radius of our least massive halo). Table 1 summarizes the main properties of our re-simulated haloes.

2.2 Visual inspection

Fig. 3 shows the projected density distribution of DM at $z = 30$ for each of our six re-simulated haloes. Their internal structure is well resolved and shows an abundant population of substructure, signatures of infalling filaments and of tidal disruption of satellite haloes. All of our haloes have well-defined centres and roughly

---

[1] Defined as the radius of a sphere with mean density equals to $\Delta_{\mathrm{vir}}\rho_{\mathrm{crit}}$, where ρ_{crit} is the critical density of the universe at a given redshift, and Δ_{vir} is the overdensity of virialized objects expected in the spherical collapse model (Bryan & Norman 1997). For the high redshifts, we consider, $\Delta_{\mathrm{vir}} = \pi^2 \simeq 178$ is equal to the virial overdensity for Einstein-de Sitter cosmologies.

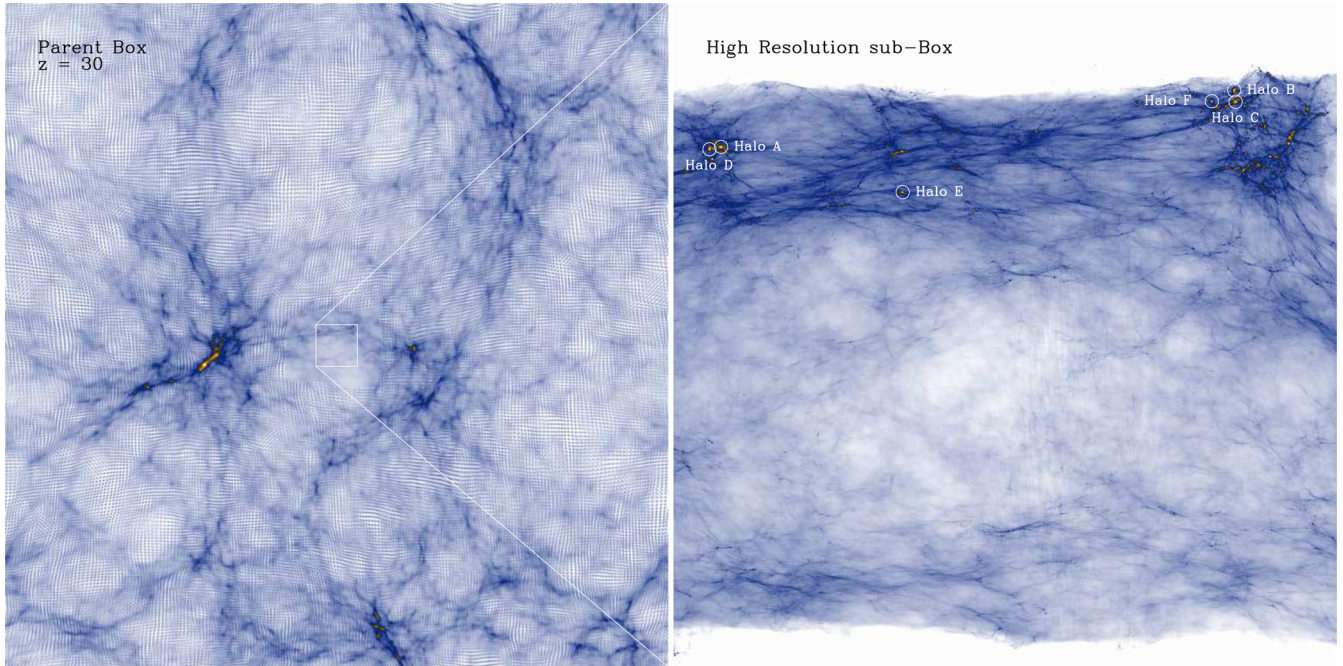**Figure 2.** The projected density of DM in our parent simulation at $z = 30$. The image displays a 1400 pc thick slab of the whole parent box (22×22 kpc; left-hand panel) and of the high-resolution subregion (1.4×1.4 pc; right-hand panel), oriented such that they contains all six haloes in our re-simulation suite (highlighted by white circles). Note the overall sparcity of collapsed structure resulting from the truncation in the initial power spectrum caused by the free streaming of neutralinos.

Table 1. Basic parameters of our high-resolution halo simulations at the final output time, $z = 30$. The free-streaming mass of the χDM model assumed is $\sim 10^{-6}\,M_\odot$ and is thus resolved with $\sim 10^4$ particles of mass $2.163 \times 10^{-10}\,M_\odot$.

Name	M_{vir} $(h^{-1}\,M_\odot)$	r_{vir} $(h^{-1}\,\mathrm{pc})$	N_{vir}	N_{hr}
Halo A	0.0271	9.62	1.25×10^8	2.02×10^8
Halo B	0.0274	9.66	1.26×10^8	2.4×10^8
Halo C	0.0159	8.06	7.36×10^7	1.16×10^7
Halo D	0.0116	7.25	5.36×10^7	8.8×10^7
Halo E	0.0127	7.48	5.88×10^7	8.6×10^7
Halo F	0.0160	8.07	7.39×10^7	1.44×10^8

spherical mass distributions. In contrast, their high-redshift progenitors are much more perturbed, displaying signatures of ongoing major mergers with several distinct structures of similar mass.

The disturbed state of these haloes is not unexpected given their complex merger histories. To illustrate this, in Fig. 4 we show images of their main progenitors at seven characteristic times during their evolution (details of our centring and tracking algorithms are provided in Appendix A). The columns in this figure correspond to the different haloes, and the rows to the outputs at redshifts 57.8, 51.6, 46.6, 42.4, 39.0, 36.0, 33.4, from top to bottom. In each panel, the virial radii of the main progenitors at this time are marked with a white circle. Interestingly, at low masses, the virial radius greatly overestimates the size (and shape) of the central collapsed region. This is due to the presence of very dense filaments, which boost the spherically averaged density in the regions surrounding the main progenitor, and is not due to the presence of virialized material. Note that this also implies that these objects are in fact much closer to the free-streaming mass than their virial mass would suggest.

The top rows, which corresponds to roughly when $M_{vir} \approx 10^{-5}\,M_\odot$, show that these haloes initially form at the centre or intersection of a network of filaments. This agrees with the classical picture of halo formation in which a density fluctuation first collapses along one axis, forming a pancake-like structure, then along a second axis forming a filament that finally collapses on to itself leading to the formation and virialization of a halo (see also Angulo, Hahn & Abel 2013, for a similar picture in WDM). Also evident in each of the top panels are several additional haloes of similar size to the main progenitor, but a dearth of lower mass systems.

By the time the main progenitors have reached 10 per cent of their final mass, they have undergone a series of major mergers with nearby structures. Notable examples are Halo B, which has of the order of 20 density peaks of comparable mass within its virial radius, and Halo E, which has a late major merger. As their mass continues to grow, our haloes start to resemble typical CDM haloes; all of them have well-defined centres, approximately spherical mass distributions, and an abundant population low-mass substructure. By the final time, they appear to be in a relatively relaxed state.

The very rapid mass growth of our haloes is highlighted also in Fig. 5, where we show the mass accretion histories (top panel) and accretion rates (bottom panel) for all six haloes. These haloes increase their mass by roughly three orders of magnitude in less than 60 Myr, a fractional accretion rate that is millions of times higher than that of cluster-sized haloes at $z = 0$ (Fakhouri, Ma, & Boylan-Kolchin 2010).

2.3 Density profiles

Before exploring the density profiles of our individual haloes, in Fig. 6, we show the *average* profiles in bins of halo mass across all output times. To construct these profiles, we first identified,
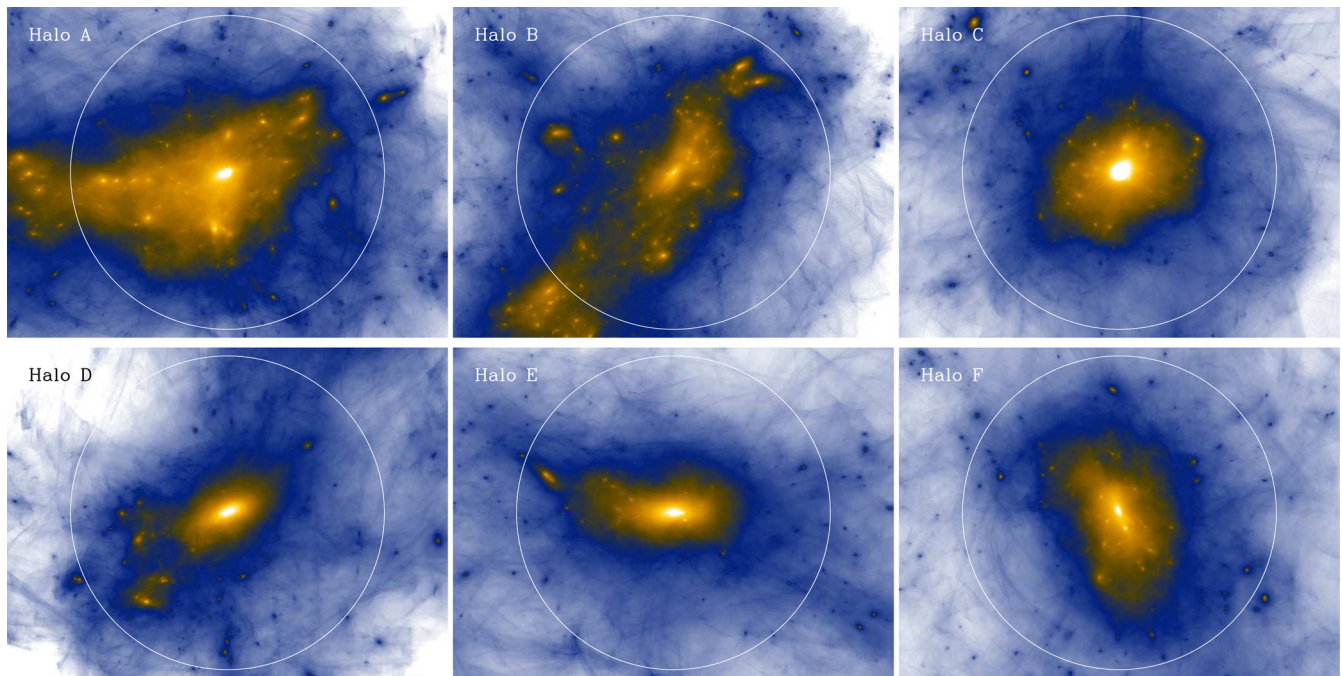
Figure 3. Six of our re-simulated DM haloes ($\sim 10^8$ particles inside the virial radius), from the most massive (top left) to the least massive (bottom right). The image shows, using a logarithmic scale, the projected density of DM times the square of the local DM velocity dispersion. The white circles indicate the virial radius of each object. These images were constructed using the method of Angulo et al. (2014) based on a tessellation of the initial DM sheet (Abel, Hahn & Kaehler 2012; Shandarin, Habib & Heitmann 2012; Hahn & Angulo 2016), and are constructed using an identical colour table in each panel

in each simulation output, all haloes with $M_{\text{vir}} > 3 \times 10^{-6}$ M$_\odot$ (corresponding to $\sim 10^4$ particles) existing in the high-resolution region of our simulations. We then compute the spherically averaged density profile for each of these haloes by summing simulation particles surrounding the halo centre in equally spaced logarithmic bins of width $\Delta \log r = 0.2$ from 0.001 to 10 pc. Finally, we add the spherically averaged density profiles after separating them into four disjoint mass bins. This substantially reduces the noise in our density estimates (each mass bin contains at least 38 haloes).

At the smallest masses, just above the free-streaming scale, the inner density profile follows closely a power law with a slope close to -1.5 (the lower diagonal dotted line in the top panel shows a pure $\rho \propto r^{-1.5}$ power law). On intermediate scales the profile exhibits a sharp decline, marking the position of the outermost caustic and highlighting the size of the collapsed region (cf also Diemer & Kravtsov 2014). Note that this scale, in agreement with our expectations from Fig. 4, is three to four times smaller than its virial radius (denoted by filled circles). As discussed above, the classical 'virial' radius overestimates the true isotropized region of the halo at the earliest times after collapse. On larger scales, extending beyond the virial radii, the density profiles become shallower, possibly reflecting the density profile of the Lagrangian 'proto-halo'.

As halo mass increases, there is a systematic change in the shape of the density profile. On small scales, the inner slope becomes shallower, approaching -1 (the NFW value) for the largest mass bin considered. Quantitatively, the measured halo mass dependence of the inner slope is in good agreement with the results of Ishiyama (2014). The values measured from the average density profiles in our simulations are $[-1.0, -1.1, -1.4, -1.6]$, respectively, for the higher to the lower mass bins considered, whereas the best-fitting relation reported by Ishiyama et al. (2010) yields $[-0.97, -1.1, -1.22, -1.34]$. These results might either suggest that the NFW profile is a dynamical attractor, or simply that haloes of different

masses form in fundamentally different ways (e.g. from protohaloes with different shapes and/or density profiles). We will investigate this next.

To explore these issues in more detail, we show the density profiles of our six re-simulated haloes in Fig. 7. In each panel, the sequence of coloured curves shows the evolution of the spherically averaged density along the main progenitor branch; red curves correspond to the highest redshifts, $z \approx 70$, and blue to redshifts closer to $z \approx 30$, the final output. The corresponding logarithmic slopes are shown in Fig. 8 for the same output times (note that the slope at radius r_i is estimated from the best power-law fit to the density measured in six adjacent radial bins).

Consistent with the picture discussed above, as our re-simulated haloes grow in mass, both the *normalization and the shape* of their spherically averaged density profiles show clear evolution with time. This implies that the profile transformation occurs on an individual halo basis rather than being a consequence of haloes of different masses being governed by different collapse and/or virialization mechanisms. Based on this, and on the images shown in Fig. 4, we may summarize a few points of interest:

(1) At the earliest times, just after the haloes emerge from the monolithic collapse of a filament, the halo's inner density profile is well described by a power law with a slope close to -1.5 (note that the exact asymptotic slope cannot be robustly determined in every case due to the intrinsic scatter in the measured profiles).

(2) All haloes evolve through a period of primarily smooth mass accretion: the outermost caustic moves closer to the virial radius, and the central density profile changes very little in either amplitude or slope. For a short time, all profiles remain close to a steep single power law.

(3) For all haloes we observe a change in the inner density slopes, which typically changes from ~-1.5 to ~-1.0 over the redshift range $z \sim 60$–40. This phase appears to coincide with the collapse
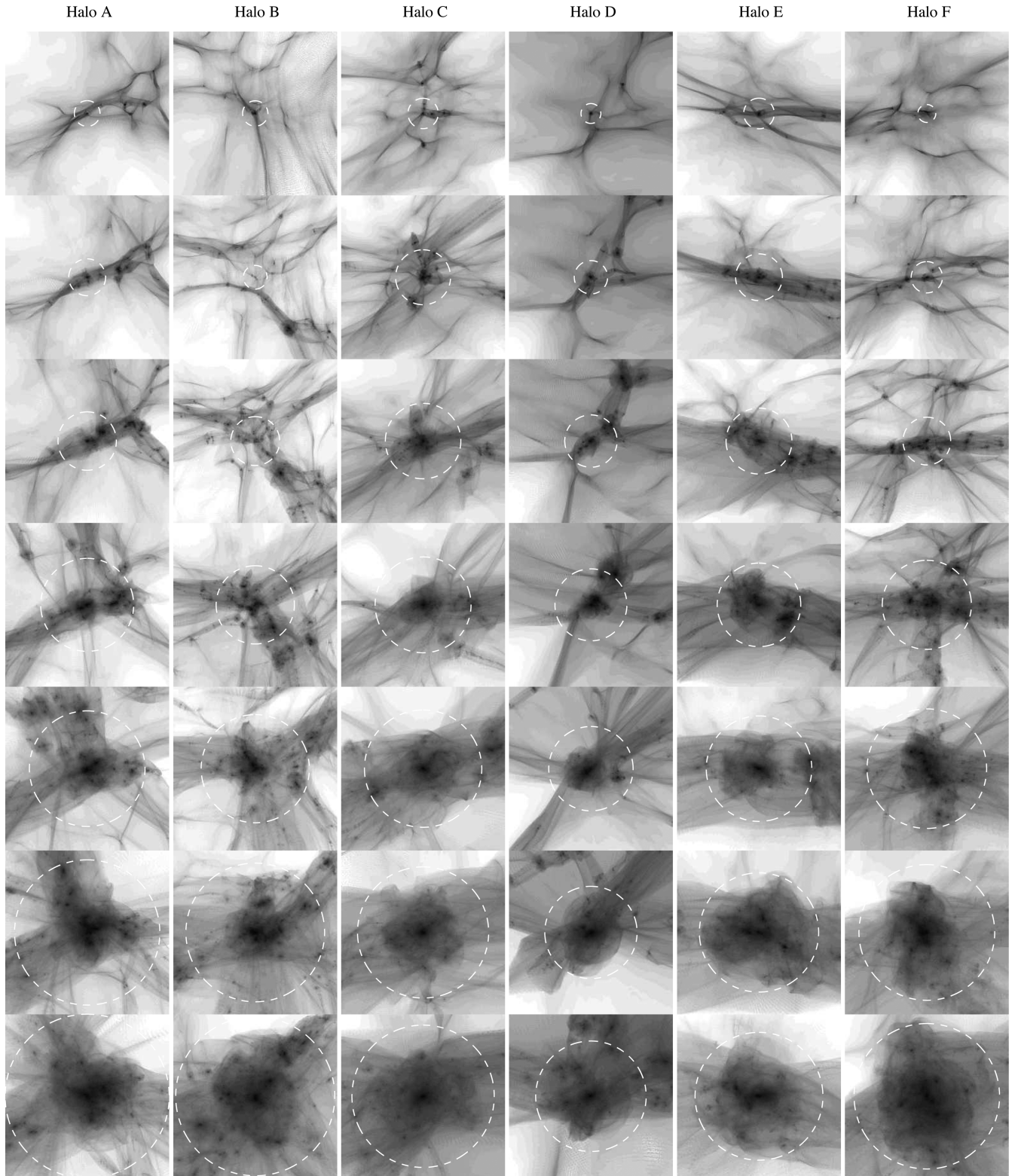
Figure 4. Snapshots of the time evolution of our six re-simulated haloes (in columns). From top to bottom, we show the mass distribution inside a region of $(12.5\,h^{-1}\,\mathrm{pc})^2$ with a projection depth of $10\,h^{-1}\,\mathrm{pc}$ at redshifts $z = 57.8, 51.6, 46.6, 42.4, 39.0, 36.0$ and 33.4 (top to bottom) centred on the main progenitor. The circles indicate the virial radius of the main progenitor at each output. The panels clearly show how the earliest progenitors form from the collapse of smooth filaments, then proceed through a phase of multiple rapid major mergers before they end up as relatively isotropic haloes of $\sim 10^{-2}\,\mathrm{M}_\odot$ at the latest times we consider.
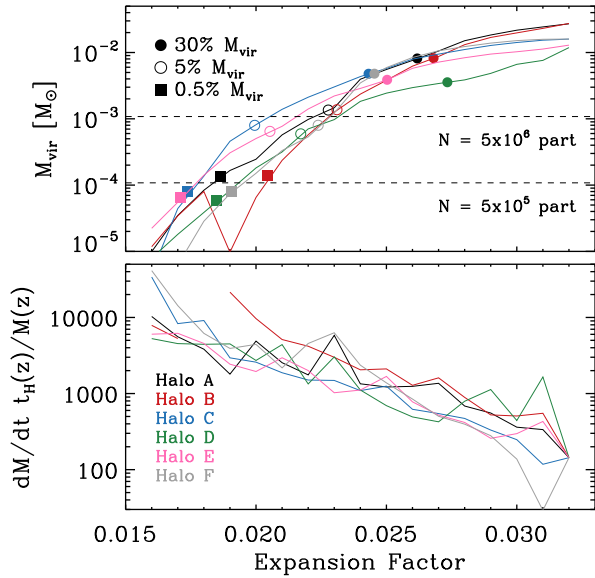
Figure 5. *Top*: the mass accretion histories of our six re-simulated haloes. The dashed horizontal lines indicate the mass scale corresponding to 10^6 and 10^7 particles. Symbols denote the point along each mass accretion history at which the main progenitor first reached 30 per cent, 5 per cent and 0.5 per cent of the final halo mass. *Bottom*: mass accretion rate, dM/dt, times the Hubble time, $t_H(z)$, divided by the current halo mass, $M(z)$. This quantity corresponds to the expected fractional increase in mass over a Hubble time, assuming a constant (instantaneous) accretion rate.
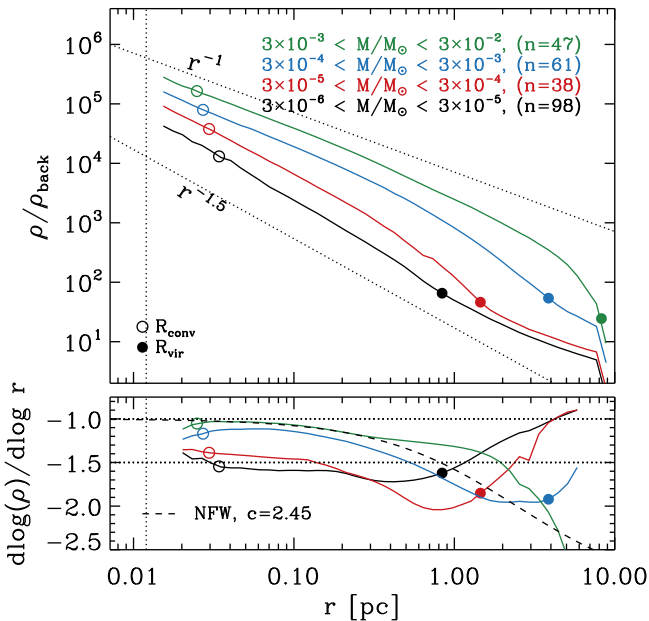

Figure 6. The average density profiles (top panel) and their logarithmic slopes (bottom panel) in bins of mass for all haloes identified (at all times) in the high-resolution region of our simulations. The range of halo masses included in each bin, as well as the number of objects in each, is indicated in the legend. The open and filled circles along each curve indicate the average convergence and virial radii, respectively. The vertical dotted line marks the formal resolution limit of our simulations, i.e. $2.8 \times \epsilon$. For comparison, the dashed line in the lower panel shows the logarithmic slope of an NFW profile with concentration $c = 2.5$. Open circles indicate the minimum scale for which we expect converged results, as estimated by the algorithm described in Power et al. (2003).

and accretion of several other haloes of similar mass, resulting in a phase of approximately simultaneous major mergers. After this period of rapid change, the functional form of the profiles appears more stable again. It is important to note that the final density profiles can be *shallower* than -1 in some cases.

In summary, our results suggest that the density profiles of the descendants of the first neutralino haloes are a consequence of the particular details of their merger history, rather than only being a manifestation of their Lagrangian peak shapes. Additionally, these results also suggest that properly resolving the first haloes and their initial merger history is necessary in order to predict the properties of more massive systems forming at later times. To elucidate the transformative effects of major mergers in shaping the density profiles of DM haloes, in the next section we explore the impact of a sequence of approximately equal mass, rapid mergers on an initially steep power-law profile.

3 CONTROLLED SIMULATIONS

As we have demonstrated in the previous section, χDM microhaloes are born with single power-law profiles and slowly transition to profiles resembling the well-known NFW form during phases of rapid mergers. We next investigate this transformation process in non-cosmological simulations in detail. Specifically, we now consider the impact of isolated and repeated mergers on an initially cuspy, spherically symmetric DM halo with an isotropic velocity distribution.

3.1 Numerical methods

We first summarize how we set up our idealized simulations of mergers of non-cosmological haloes. Specifically, the density profiles we assume, how we sample them with *N*-body particles, and how we set up the mergers of several of such haloes.

3.1.1 Initial conditions

For our simplified halo models, we assume an initial power-law density profile, truncated at large radii, of the form

$$\rho(r) = \rho_s \left(\frac{r}{r_s} \right)^{-\gamma} \mathrm{erfc}[\kappa(r/r_s - 1)]. \quad (2)$$

Here, ρ_s and r_s are the arbitrary scaling variables of density and radius, respectively, and κ defines the cut-off scale. We consider three power-law indices, $\gamma = 1.0$, 1.5 and 1.9, and in all cases adopt $\kappa = 2$ and $r_s = R_{vir}$; ρ_s is chosen to fix the halo mass to the desired value. In addition to these scale-free models, we also consider haloes with a Hernquist density profile (Hernquist 1990) with a concentration parameter of $R_{vir}/r_s = 2.5$. We show the distribution functions associated with each of these four cases in Fig. B1 of Appendix B1.

Each of our models samples the density distribution using 10^6 particles.[2] Velocity magnitudes, v, are drawn directly from an isotropic distribution function, which we calculate using Eddington's formula (e.g. Binney & Tremaine 2008):

$$f(E) = \frac{1}{\sqrt{8}\pi^2} \left[\int_0^E \frac{d^2\rho}{d\Psi^2} \frac{d\Psi}{\sqrt{E - \Psi}} + \frac{1}{\sqrt{E}} \left(\frac{d\rho}{d\Psi} \right)_{\Psi=0} \right]. \quad (3)$$

---

[2] Note that this refers to the total particle number within the virial radius. Because the mass model extends to slightly larger radii, the total number of particles used for each halo is slightly larger.
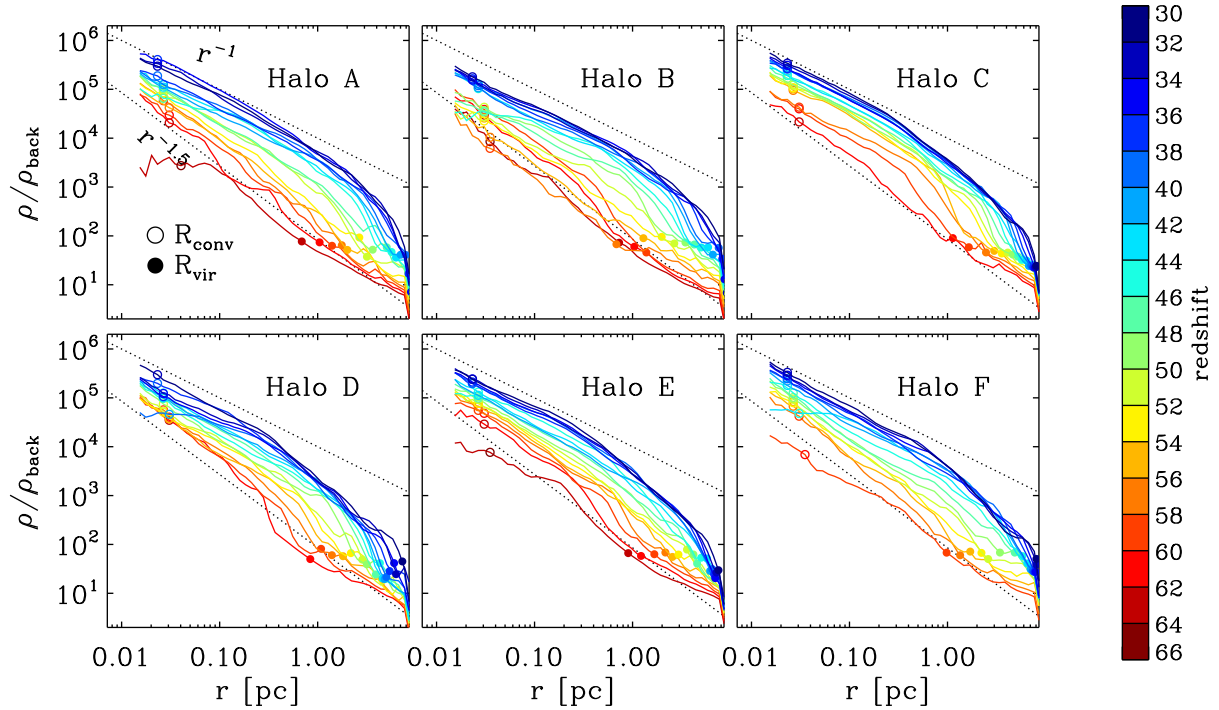
Figure 7. The evolution of the spherically averaged density profiles for the main progenitor of each of our six haloes. Different colours show results for different redshifts, as indicated by the colour bar on the right-hand side. Densities are normalized by the background density at each redshift, and radii are expressed as the comoving distance to the halo centre. The dotted lines highlight two power-law profiles, $\rho \propto r^{-1.5}$ and r^{-1}. Filled circles along each curve indicate the virial radius of the main progenitor and open circles the convergence radius (see Power et al. 2003).
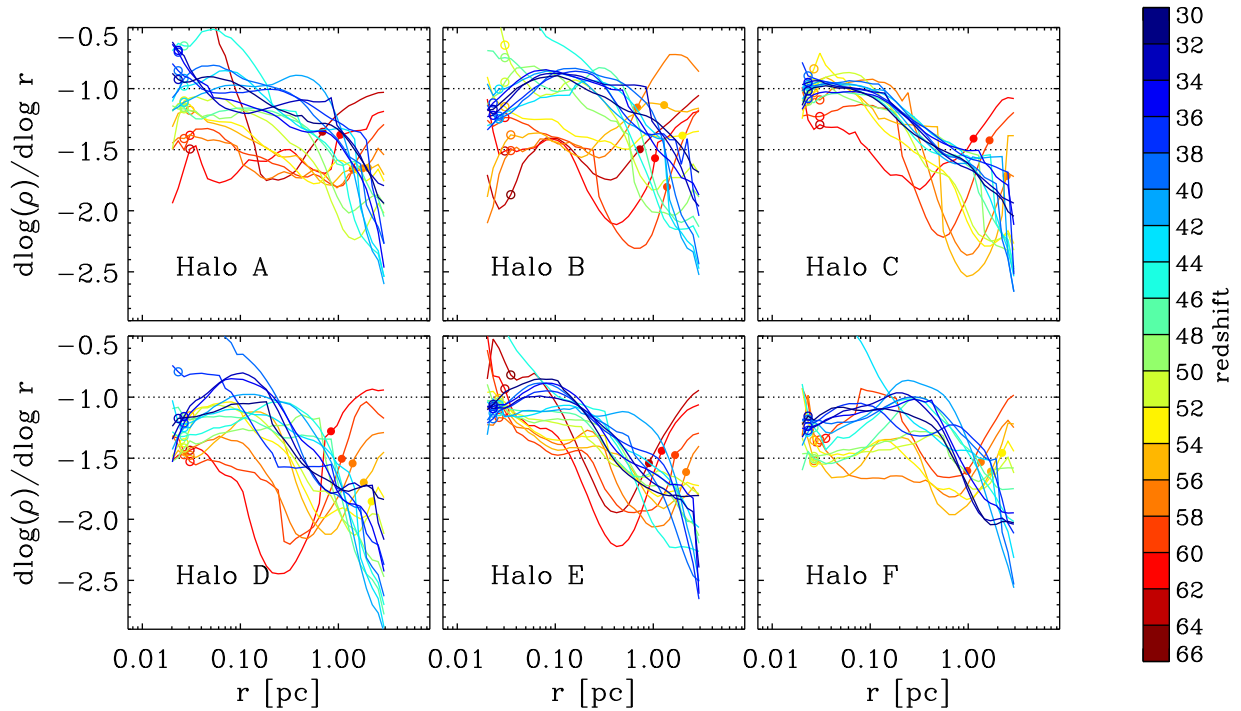

Figure 8. Same as Fig. 7 but showing the logarithmic slope of the density profiles.

Here, $E \equiv -\Phi(r) - \frac{1}{2}v^2$ is the relative energy and $\Psi \equiv -\Phi$ the relative potential. Particle radii and velocities are then assigned random orientations such that the resulting halo is isotropic in both position and velocity space. We note that this procedure yields more accurate

and robust results than the widely used local Maxwellian approximation (see also Kazantzidis et al. 2004). We describe our procedure for setting up these initial conditions in more detail in Appendix B1, and test the stability of our model haloes in Appendix B2.
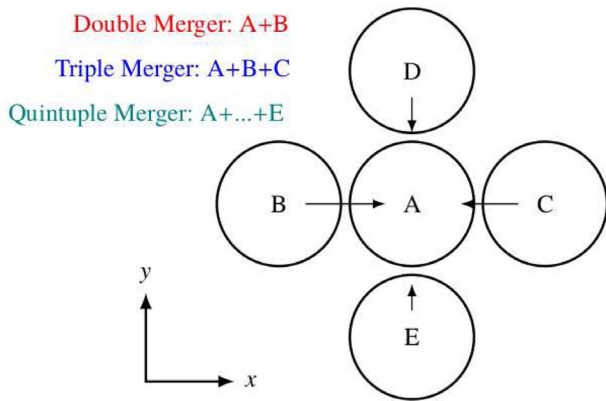
Figure 9. Diagram showing the possible initial configurations of our merger simulations. All haloes are initially placed on the *x*–*y* plane, and are displaced by two virial radii from the central halo A. Arrows indicate the magnitude and direction of the initial velocity vector of the haloes: all are set on radial orbits with velocities equal to 100 per cent, 75 per cent, 50 per cent and 25 per cent of the escape speed measured at the virial radius of halo A.

3.1.2 Model parameters and initial set-up of the mergers

To explore the impact of multiple major mergers on the internal density profile of a halo, we simulate a sequence of head-on mergers of identical, spherically symmetric haloes generated using the procedure described above. Fig. 9 shows the merger configurations, of which we will consider three cases: (1) a binary merger between haloes A and B, (2) a triple merger between haloes A, B and C and (3) a quintuple merger between all five haloes. Initially, the centres of all haloes lie on the same plane and are separated from halo A by $2 \times R_{\text{vir}}$.

We choose a coordinate system so that halo A is initially at rest, and set the remaining haloes on radial orbits with relative velocities of $v_{\text{rel}} = -v_{\text{esc}}$, $-3/4\,v_{\text{rel}}$, $-1/2\,v_{\text{rel}}$ and $-1/4\,v_{\text{rel}}$ for haloes B, C, D and E, respectively. Here, v_{esc} is the nominal escape speed measured at the virial radius of Halo A. The differences in the relative velocities of the haloes ensure that the mergers are not synchronized, but also that each occurs before the system has had time to dynamically recover from prior mergers. Although other configurations are clearly possible, this choice is motivated by the very violent merger histories of our neutralino haloes with near-radial orbits.

All merger simulations were carried out using P-GADGET3, the same code that was used for our cosmological runs. Forces were computed using only the Tree algorithm, with open boundary conditions within a static (non-expanding) background. The softening length was set to $\epsilon = 0.3$ kpc, approximately 0.2 per cent of the initial virial radius of each halo. Forces are therefore exactly Newtonian for separations larger than $2.8 \times \epsilon = 0.84$ kpc. All simulations were evolved for 15 Gyr ($\sim$8 dynamical times), and employed approximately 9000 adaptive time-steps. We output the particle data at 16 different times, with the last 5 separated by 0.01 Gyr. To reduce noise, the final results of these simulations will be presented as an average over those five final output times. All models are initialized to have a virial mass of $10^{12}\,\text{M}_\odot$ and a virial radius of 162.2 kpc. Although this is a very different mass scale than that of our neutralino haloes, the scale-free nature of gravity guarantees that this choice is irrelevant.
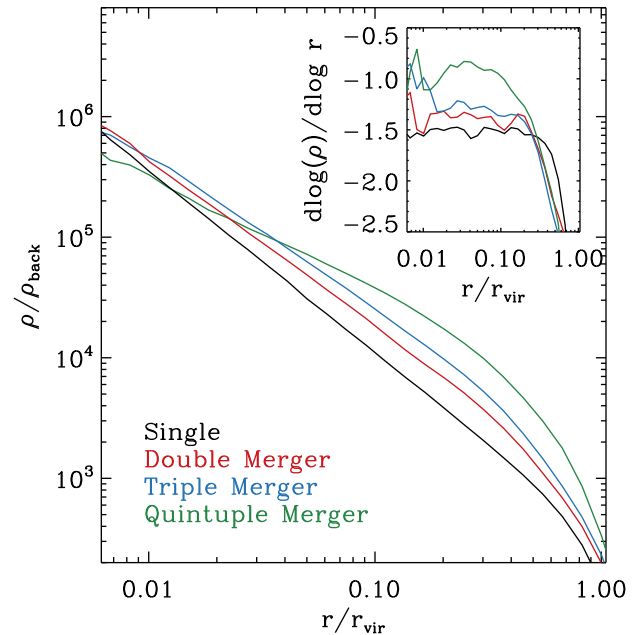

Figure 10. The density profiles, in units of the background density, of the final remnants of equal-mass mergers between haloes with initial power-law density profiles with $\gamma = 1.5$, cf equation (2). Different colours show the results for an isolated halo (black), and for two, three and five mergers (red, blue and green, respectively). The inset shows the logarithmic density slopes. In both plots, the *x*-axis has been scaled by the initial virial radius of halo A.

3.2 Merger remnants for $\gamma = 1.5$ profiles

We first study the outcome of the merger of up to five such idealized haloes that are initially given by the truncated single power-law profiles given in equation (2) with a slope of $\gamma = 1.5$. Specifically, we investigate how their density profiles are changed as a result of the mergers and focus on how the inner asymptotic slope evolves away from the initial value of γ.

In Fig. 10 we show the remnant density profiles for mergers between initially isotropic haloes with $\gamma = 1.5$ power-law density cusps (the initial density profiles in this case are a good match to those of the first generation of neutralino haloes). Lines of different colours correspond to the different merger configurations discussed above.

The most striking result seen here is that the final profile departs significantly from its original power-law form, and exhibits an inner slope that becomes systematically shallower as the number of mergers increases. This is best appreciated in the inset plot, which displays the logarithmic slopes of the profiles. For the binary merger, the initial power-law index of -1.5 has decreased slightly, to $\sim$$-1.4$, whereas for the quintuple merger it has decreased to $\sim$$-0.8$, a value much closer to (and even lower than) the asymptotic slope of the NFW profile. At the same time, the outer slope becomes steeper. Overall, the homology of the original density profile is broken and its final shape depends sensitively on the particular details of its merger history. This is qualitatively very different than the outcome of mergers between NFW haloes, which primarily affect the profile's concentration, but not its shape (e.g. Kazantzidis, Zentner & Kravtsov 2006). In addition, there is no single asymptotic value for the inner slope, which apparently disfavours the interpretation that the NFW profile is a natural outcome of major mergers.
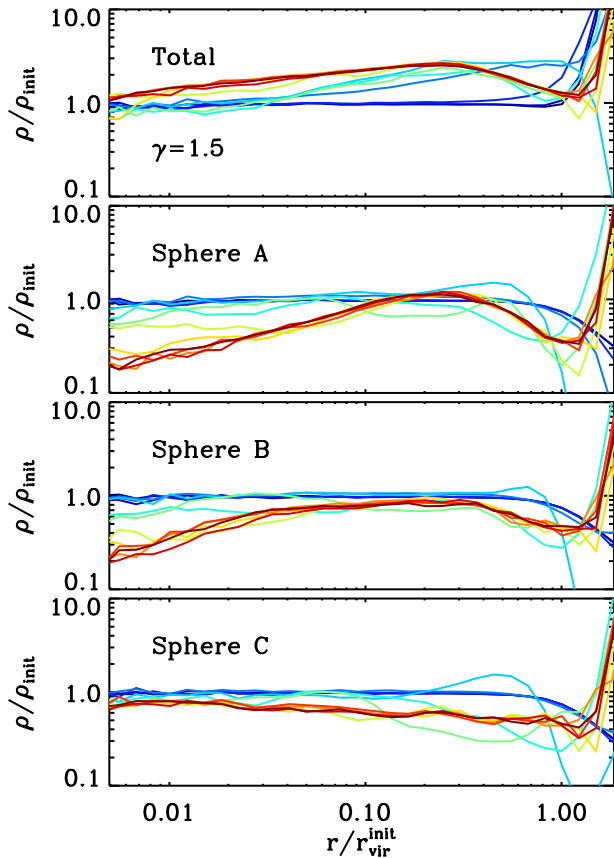
Figure 11. The final density profile, in units of the initial value, of the triple $\gamma = 1.5$ merger simulation. The top plot shows the results for all particles, whereas each of the lower panels focuses on the mass contributed by each of the three progenitors, as indicated by the legend. In each panel, coloured lines indicate the results at different output times; dark blue corresponds to the initial times, whereas dark red corresponds to the final times.

We now take a closer look at the triple merger case by following the time evolution of the density profile, separately considering the particles initially associated with each progenitor. Fig. 11 shows the spherically averaged density profiles after normalizing the initial analytic profile. Different panels, from top to bottom, show results for all particles, as well as for particles belonging to Haloes A, B and C, respectively. For each particle subset, and at every output time, we have recomputed the centre of mass before calculating $\rho(r)$.

We can see clearly that the final density profile is not simply a rescaled version of the initial one, reinforcing the results discussed above. Furthermore, the distribution of particles that originated from each progenitor also changes. For Haloes A and B, the first two to collide, the central densities decrease significantly and rapidly, by about a factor of 5 in less than $\Delta t = 1$ Gyr. The outer parts also suffer a major decrease in density. Because the density does not increase above the initial value at any radius, the removed particles have necessarily moved beyond the initial halo boundaries (causing the quantity plotted to reach values above unity for $r > r_{\mathrm{vir}}$). On the other hand, particles from Halo C appear to have suffered a qualitatively different transformation: densities decrease on all scales, but only slightly so. In fact, particles from Halo C dominate the central regions of the final halo. We note that this, however, is not a universal behaviour. For other merger configurations, Haloes A or B end up dominating the central regions, while the last sphere accreted is
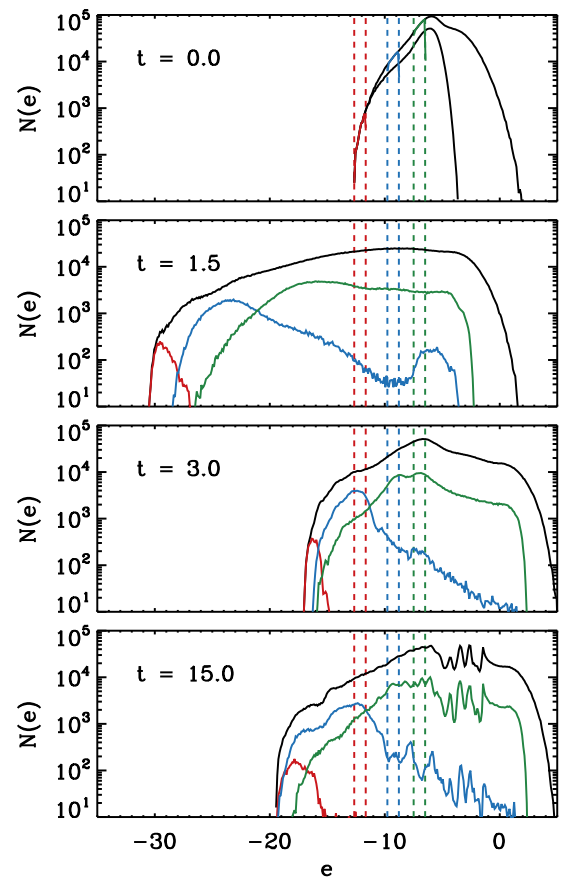

Figure 12. Time evolution of the distribution of energies of particles in the triple merger of $\gamma = 1.5$ spheres. The top panel shows the initial configuration. The second panel, $t = 1.5$, corresponds to the time when the potential reaches its minimum value. The next panel, $t = 3.0$, corresponds to when the potential reaches a local maximum, as the merger remnants recede. The black line shows the distribution for all particles involved in the mergers, whereas coloured lines follow the distribution of only those particles inside three initially narrow energy bins, indicated by the vertical dashed lines of the same colour.

more strongly disrupted. Thus, the transformation suffered by a particular sphere seems to depend on the particular details of the merger. What seems ubiquitous, however, is the emergence of an inflection point in the total profile: a scale above and below which the distribution of densities decreases. In the following section, we will explore the origin of these transformations in more detail.

3.3 Energy distribution and violent relaxation

During major mergers, the relative motion of large amounts of mass leads to large temporal variations in the gravitational potential. In a process known as violent relaxation (Lynden-Bell 1967), these potential fluctuations change the energies of individual particles, resulting in a final equilibrium state whose mass distribution can be substantially different than the initial one. We argue that it is indeed violent relaxation that drives the evolution of the density profile of the merger remnant. In this section, we provide evidence for this scenario in terms of the evolution of the particle energy distribution function as well as the temporal evolution of the central potential during the merger.

In Fig. 12, we plot the time evolution of distribution of energies for particles involved in the triple merger. The initial distributions

for the whole system and for the central sphere are shown in the top panel using thick and thin solid black lines, respectively. Coloured lines follow the energy distributions of particles inside three narrow bins of initial energy, marked in each panel using vertical dashed lines of similar colour. Green lines follow an initially weakly bound group of particles, blue lines correspond to particles with average energy and red lines to the most bound particles.

As expected for a system undergoing violent relaxation, the initially narrow energy distributions broaden significantly as a result of the mergers. During these events, the potential energy fluctuates (as we will explicitly show below) but the total energy must remain constant; the system responds by increasing or decreasing the kinetic energy of individual particles as it settles towards a new equilibrium state. This oscillatory behaviour modifies the energies of individual particles thereby broadening the overall distributions. The most bound particles become even more tightly bound, whereas many weakly bound particles gain enough kinetic energy to become unbound. Although not shown here, the broadening of the energy distributions is more substantial for mergers involving a larger number of progenitors, which drive larger fluctuations in the underlying gravitational potential of the system.

At $t = 1.5$ (which coincides with the minimum value of the potential energy), the energy distributions become very broad, and exhibit a much higher absolute mean. The increased depth of the gravitational potential offers new energy states, making it possible for particles to become more tightly bound. At $t = 3$, when the potential has decreased substantially, the average and the dispersion in the energy distributions also decrease, as the merger remnants are partially destroyed and no longer contribute to large potential fluctuations. At this point, some particles reach positive energies and escape the system entirely. By the final time, the velocity dispersion of particles stabilizes but, due to the increased mass of the system as a whole, the binding energy of all three groups has increased (i.e. become more negative). Furthermore, the initially smooth distribution develops oscillatory features at low energies, which are imprinted by the particular merger configuration.

These results suggest that violent relaxation can drive large changes in mass profiles of haloes, ultimately transforming their density profiles from one form to another. To highlight this, in Fig. 13 we plot the time evolution of the logarithmic density slope (top panel), the central gravitational potential (middle panel) and of the central velocity dispersion (bottom panel). The latter two quantities were computed in the range $0.01 < r/R_{\mathrm{vir}} < 0.05$. Differently coloured lines show the results for the evolution of an isolated halo (black), and for three merger configurations considered, as indicated in the legend.

We can see that while the isolated halo shows an invariant slope and potential at all times, the various mergers display strong variations in all quantities. For all configurations, there are several rapid increases in Ψ (by factors of 3–8, depending on the number of systems involved in the merger) as the merging systems approach one another. Ψ reaches its maximum during pericentric passages, and decreases as the merger remnants recede. The amplitude of fluctuations in the potential is rapidly suppressed in subsequent pericentric passages, owing to phase-mixing (violent relaxation is self-limiting). The whole system then approaches a new equilibrium and the gravitational potential stabilizes at a value in between the initial and maximum values. We can see that variations in the potential coincide with variations in the specific kinetic energy (or σ) as well as in the density slope. This supports our previous conjecture that major mergers are directly responsible for the transformation of the density profile observed in our cosmological simulations.
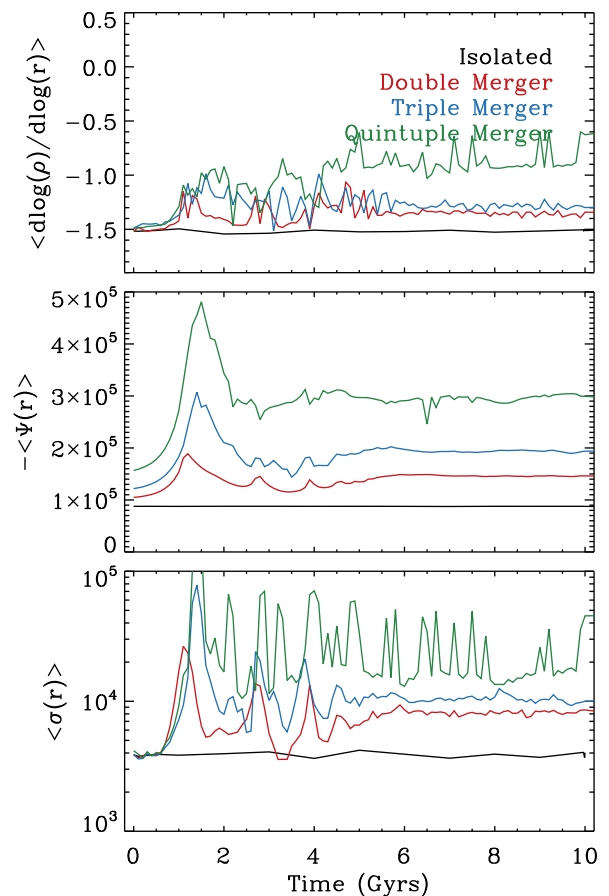

Figure 13. The time evolution of the average density profile slope (top panel), gravitational potential (middle panel) and velocity dispersion (bottom panel) of merger remnants of halo models with $\gamma = 1.5$. The average density slope is measured by fitting a power law over the range $0.01 < r/R_{\mathrm{vir}} < 0.1$ to each measure density profile, while the average potential and velocity dispersion were computed over a smaller radial range, $0.01 < r/R_{\mathrm{vir}} < 0.05$.

3.4 Merger remnants for other density slopes

We saw above that violent relaxation can transform initially steep density cusps into substantially shallower ones which provides a natural explanation for why the initial $r^{-1.5}$ profiles should not survive through phases of multiple major mergers. In the cosmological simulations of the first part of the paper, the profiles approached a significantly shallower inner slope and in particular the broken power-law profiles of the NFW type during later stages of evolution. A remaining open question is thus whether there is a natural end-point to the evolution of the density profiles or whether slopes can be made arbitrarily shallow through violent relaxation processes. We will study this aspect in this section by investigating the role of the exact value of the initial slope of the single power-law profiles on the profile of the merger remnant. Furthermore, we will investigate whether broken power-law profiles could serve as a natural end-point of such a process by being particularly resilient to further mergers.

Indeed, the magnitude of the transformation depends sensitively on both the number of mergers as well as on initial density profiles of the merging systems. Greater numbers of mergers lead to larger potential fluctuations, whereas steeper cusps have deeper potentials, which are more resilient to potential fluctuations of similar
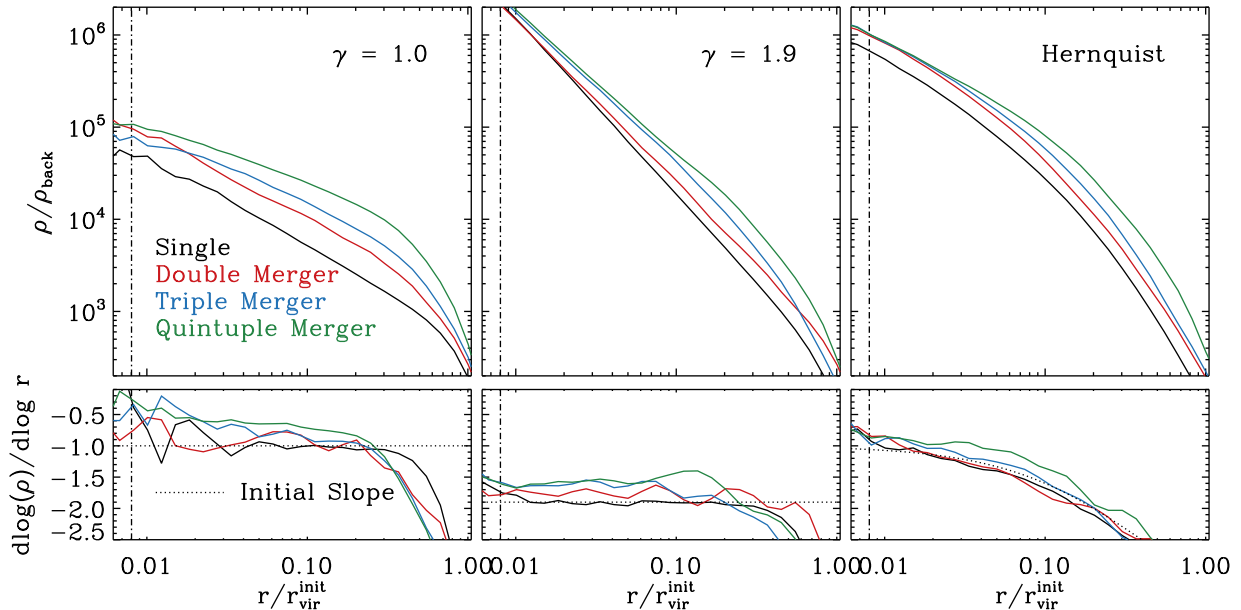
Figure 14. The final density profiles for our (non-cosmological) simulations of equal-mass mergers. The top panels show the spherically averaged density in units of the background density; bottom panels show the corresponding logarithmic slopes. Each column displays results for models with different initial density profiles, with different colours corresponding to different merger scenarios, as indicated in the legend. The ordinate plots the radial variable in units of the initial virial radius of each halo.

magnitude. This can be clearly seen in Fig. 14, where we plot the density profiles of merger remnants whose progenitors had power-law density profiles with slopes of $\gamma = 1$ (left), 1.9 (middle) and for Hernquist density profiles (right). As in previous plots, different colours show results for different merger configurations.

For both power-law models, the behaviour is qualitatively similar to the $\gamma = 1.5$ case discussed above: multiple equal-mass mergers result in shallower remnant profiles, with the largest changes seen for cases with the highest number of mergers. The relative change in inner slope appears to correlate with the initial value: for $\gamma = 1.0$, 1.5 and 1.9, the fractional change in slope is 80, 50 and 30 per cent, respectively. This is because violent relaxation only occurs when fluctuations in the gravitational potential are of the same order as the self-binding potential of the system, which is substantially larger for systems with steeper inner density cusps. On the other hand, changes to the Hernquist models are comparatively smaller. Even for the quintuple merger scenario, the relative changes to the inner slope are only ∼10 per cent, comparable to the statistical noise in our density estimates. The stability of the Hernquist model to violent merging is consistent with previous studies on the impact of mergers on the equilibrium structure of DM haloes (e.g. Boylan-Kolchin & Ma 2004; Kazantzidis et al. 2006; El-Zant 2008). Note that in the case of Hernquist or NFW profiles, the central potential is considerably deeper than in the single power-law profiles considered above. The deeper potential implies that mergers induce smaller relative variations, which explains the smaller changes in the final density profile.

The above results emphasize the importance of properly modelling the initial collapse of DM haloes near the free-streaming scale: for identical merger histories, halo profiles depend sensitively on the profiles of their progenitors. Additionally, a value of −1 for the inner slope does not stand out as a special case in this context, and the final halo can, in principle, acquire a range of values depending on the precise details of its accretion history and progenitor population.

4 DISCUSSION AND CONCLUSIONS

Attempts to explain the origin of the universal broken power-law density profiles (e.g. equation 1) of collisionless DM haloes have permeated the literature on cosmological structure formation ever since their discovery by Navarro et al. (1996, 1997). A complete physical picture of their origin, however, has not yet emerged. In this article, we approach this subject from two angles: first from simulations of structure formation in a χDM cosmology, and, secondly, from a set of well-controlled equal-mass merger simulations of power-law haloes.

In a χDM universe, hierarchical growth begins at about an earth mass, which is the mass of the very first haloes to collapse and the mass of the smallest haloes to form at any cosmic epoch. Therefore, this situation provides a well-defined scale to be resolved by numerical simulations, and thus a unique test for the self-similarity of DM halo density profiles. In this paper, we focus on the formation and evolution of six ∼0.01–0.02 $M_\odot$ haloes using the high-resolution zoom technique. We simulate these haloes from $z = 399$ to $z = 30$, tracing their mass growth over more than four orders of magnitude, and study the evolution of their density profiles and assembly histories. We chose these haloes to reside in a not particularly dense environment inside of a large cosmological volume in order to focus on typical microhaloes rather than the high-sigma peaks.

In agreement with previous studies (Diemand et al. 2005; Ishiyama et al. 2010; Anderhalden & Diemand 2013; Ishiyama 2014), we found that this first generation of χDM haloes have spherically averaged density profiles that are well described by single power laws, $\rho \propto r^{-1.5}$, inconsistent with the gently curving NFW profiles that are ubiquitous at later times and at much larger halo masses. We then observed that, as our haloes grow in mass, all of them experienced a significant reduction in their inner slope (even becoming shallower than −1 in some cases). This transformation occurs rapidly, and appears to coincide with an early evolutionary phase in which major mergers are particularly abundant. The final outcome is that all of them display an inner, shallower slope close

to −1 as well as a steeper outer profile. Even at the latest times we considered, they are, while being close, however, still not particularly well fit by NFW profiles arguably owing to the rapid assembly phase in which they still find themselves.

Motivated by this, we explored the impact of major mergers on halo density profiles using a suite of non-cosmological simulations of idealized major mergers. We considered equal-mass mergers with a range of multiplicities (from binary mergers up to mergers involving five identical haloes) as well as a range of initial density profiles. We showed that, in all configurations, temporal variations in the gravitational potential induced by the mergers lead to a significant modification of the initial density profile. This is a somewhat unexpected outcome, as it has been argued several times (Boylan-Kolchin & Ma 2004; Kazantzidis et al. 2006; El-Zant 2008) that mergers do not change density profiles (but see Laporte & White 2015), but it is consistent with the recent analysis of Ogiya, Nagai & Ishiyama (2016).

More specifically, we find that major mergers transform the entire halo profile in the following ways:

(i) A higher number of merger progenitors drives larger fluctuations in the gravitational potential, resulting in more substantial reduction of the inner density slope.

(ii) There is no clear limiting inner slope, and the final profile can be significantly shallower than r^{-1}.

(iii) Shallower progenitor profiles are more vulnerable to the effects of mergers, due to their lower self-binding energies.

(iv) Mergers establish an outer envelope that leads to a broken power-law profile with a distinct inner and outer slopes.

(v) If the progenitor profile is a broken power law, the end result is a profile whose shape is largely insensitive to its merger history (which make our findings compatible with previous published results).

The general picture that emerges from these simulations is very clear: haloes are born as single power-law profiles with a slope close to −1.5 which then evolve through major mergers to more complicated profiles with a shallower inner and a steeper outer profile. Once a broken power-law profile is established, it becomes resilient to further mergers.

It is interesting to note that fluctuating potentials have been suggested as the origin of cusp-core transformations in dwarf galaxies (e.g. Pontzen & Governato 2012; Zolotov et al. 2012; Ogiya & Mori 2014; El-Zant, Freundlich & Combes 2016), and that major mergers can significantly alter the central structure of elliptical galaxies (e.g. Hilz et al. 2012; Hilz, Naab & Ostriker 2013). Although the physical origin of fluctuating potentials and mergers is completely different, the same physical processes appear to be acting on shaping galaxies as well as subsolar DM haloes.

It is also interesting to conjecture about the Milky Way sized descendant haloes of neutralino haloes based on the evidence presented in this paper. We showed that the initial collapse establishes a simple profile, $\rho \propto r^{-1.5}$. These power-law profiles are unstable to strong perturbations and can be made shallower by subsequent rapid major mergers. There is no reason preventing haloes to emerge from the initial period of major mergers significantly shallower than −1; however, the particular shape of the DM mass spectrum appears not to allow enough mergers for this to happen to a typical halo. As haloes grow in mass and the frequency of major mergers decreases, a more persistent, broken power-law density profile emerges. Subsequent mass growth and major and minor mergers are not expected to modify this profile much further. Therefore, we speculate that in a χDM scenario, even galactic-sized haloes might show some

variance in their inner density slope – some of them being shallower than −1, but some of them steeper – resulting from the diversity of their early merger history. In the future, larger statistical samples in larger simulation volumes, as well as over more extended periods of mass growth, will be able to test the validity of this scenario.

We believe that the analysis we conducted in this article has important implications for the interpretation of the universal structure of DM haloes. However, several important questions remain open:

(i) How are the self-similar power-law profiles connected to the initial (smooth) peak profile from which they form? Using different initial peak profiles in numerical experiments it may be possible to connect the mass profiles of these haloes to those of their initial (Lagrangian) peaks (see e.g. Vogelsberger, Mohayaee & White 2011), and investigate the dependence of the power-law index on the cut-off scale, power spectrum slope and cosmology.

(ii) What is the dependence of the final halo on the cut-off scale? The frequency and mass ratios of mergers that a typical halo will undergo during its initial evolutionary phase are directly related to the slope and variance of the power spectrum at the cut-off scale. Simulations of the same objects but embedded in different large-scale fluctuations will be able to investigate in more detail the degree to which an initial profile can be transformed for a given DM particle mass.

(iii) Our results suggest that a simple overdensity-based criterion for identifying haloes largely overestimates their truly isotropized and virialized regions at very early times. A robust definition of what constitutes a virialized object, and how it can be identified and delineated reliably in a simulation, should be explored in future studies of neutralino halo formation.

(iv) The most puzzling open question, however, is why standard CDM *N*-body simulations so consistently produce haloes whose mass profiles resemble the NFW profile. Future simulations with improved mass and force resolution, as well as alternative methods with reduced noise, might be able to connect the apparently contradictory results of χDM, WDM and standard (perfectly cold) CDM simulations. However, our results already indicate the importance of resolving the correct number of major mergers in the early halo evolution.

We plan to address these questions in future work, and hope that our results motivate others to investigate cosmological structure formation near the free-streaming scale.

ACKNOWLEDGEMENTS

REFERENCES

Abel T., Hahn O., Kaehler R., 2012, MNRAS, 427, 61
Anderhalden D., Diemand J., 2013, J. Cosmology Astropart. Phys., 4, 009
Angulo R. E., White S. D. M., 2010, MNRAS, 401, 1796
Angulo R. E., Hahn O., Abel T., 2013, MNRAS, 434, 1756
Angulo R. E., Chen R., Hilbert S., Abel T., 2014, MNRAS, 444, 2925
Baushev A. N., 2015, Astropart. Phys., 62, 47
Bertschinger E., 1985, ApJS, 58, 39

Binney J., Tremaine S., 2008, Galactic Dynamics, 2nd edn. Princeton Univ.
    Press, Princeton, NJ
Boylan-Kolchin M., Ma C.-P., 2004, MNRAS, 349, 1117
Bryan G. L., Norman M. L., 1997, in Clarke D. A., West M. J., eds,
    ASP Conf. Ser., Vol. 123, Computational Astrophysics; 12th Kingston
    Meeting on Theoretical Astrophysics. Astron. Soc. Pac., San Francisco,
    p. 363
Bullock J. S., Kolatt T. S., Sigad Y., Somerville R. S., Kravtsov A. V., Klypin
    A. A., Primack J. R., Dekel A., 2001, MNRAS, 321, 559
Cole S., Lacey C., 1996, MNRAS, 281, 716
Dalal N., Lithwick Y., Kuhlen M., 2010, preprint (arXiv:1010.2539)
Davis M., Efstathiou G., Frenk C. S., White S. D. M., 1985, ApJ, 292, 371
Diemand J., Moore B., Stadel J., 2005, Nature, 433, 389
Diemand J., Kuhlen M., Madau P., 2007, ApJ, 667, 859
Diemer B., Kravtsov A. V., 2014, ApJ, 789, 1
Dubinski J., Carlberg R. G., 1991, ApJ, 378, 496
El-Zant A. A., 2008, ApJ, 681, 1058
El-Zant A. A., Freundlich J., Combes F., 2016, MNRAS, 461, 1745
Fakhouri O., Ma C., Boylan-Kolchin M., 2010, MNRAS, 406, 2267
Fillmore J. A., Goldreich P., 1984, ApJ, 281, 1
Frenk C. S., White S. D. M., Davis M., Efstathiou G., 1988, ApJ, 327, 507
Gao L., Navarro J. F., Frenk C. S., Jenkins A., Springel V., White S. D. M.,
    2012, MNRAS, 425, 2169
Gelb J. M., Bertschinger E., 1994, ApJ, 436, 467
Green A. M., Hofmann S., Schwarz D. J., 2004, MNRAS, 353, L23
Gunn J. E., Gott J. R., III, 1972, ApJ, 176, 1
Hahn O., Abel T., 2011, MNRAS, 415, 2101
Hahn O., Angulo R. E., 2016, MNRAS, 455, 1115
Hernquist L., 1990, ApJ, 356, 359
Hilz M., Naab T., Ostriker J. P., Thomas J., Burkert A., Jesseit R., 2012,
    MNRAS, 425, 3119
Hilz M., Naab T., Ostriker J. P., 2013, MNRAS, 429, 2924
Hofmann S., Schwarz D. J., Stöcker H., 2001, Phys. Rev. D, 64, 083507
Huss A., Jain B., Steinmetz M., 1999, ApJ, 517, 64
Ishiyama T., 2014, ApJ, 788, 27
Ishiyama T., Makino J., Ebisuzaki T., 2010, ApJ, 723, L195
Juan E., Salvador-Solé E., Domènech G., Manrique A., 2014, MNRAS, 439,
    719
Kazantzidis S., Mayer L., Mastropietro C., Diemand J., Stadel J., Moore B.,
    2004, ApJ, 608, 663
Kazantzidis S., Zentner A. R., Kravtsov A. V., 2006, ApJ, 641, 647
Laporte C. F. P., White S. D. M., 2015, MNRAS, 451, 1177
Lentz E. W., Quinn T. R., Rosenberg L. J., 2016, ApJ, 822, 89
Lovell M. R. et al., 2012, MNRAS, 420, 2318
Ludlow A. D. et al., 2013, MNRAS, 432, 1103
Lynden-Bell D., 1967, MNRAS, 136, 101
Navarro J. F., Frenk C. S., White S. D. M., 1996, ApJ, 462, 563
Navarro J. F., Frenk C. S., White S. D. M., 1997, ApJ, 490, 493
Navarro J. F. et al., 2010, MNRAS, 402, 21
Ogiya G., Mori M., 2014, ApJ, 793, 46
Ogiya G., Nagai D., Ishiyama T., 2016, MNRAS, 461, 3385
Pontzen A., Governato F., 2012, MNRAS, 421, 3464
Pontzen A., Governato F., 2013, MNRAS, 430, 121
Power C., Navarro J. F., Jenkins A., Frenk C. S., White S. D. M., Springel
    V., Stadel J., Quinn T., 2003, MNRAS, 338, 14
Shandarin S., Habib S., Heitmann K., 2012, Phys. Rev. D, 85, 083005
Springel V. et al., 2008, MNRAS, 391, 1685
Taylor J. E., Navarro J. F., 2001, ApJ, 563, 483
Vogelsberger M., Mohayaee R., White S. D. M., 2011, MNRAS, 414, 3044
Wang J., White S. D. M., 2007, MNRAS, 380, 93
Zolotov A. et al., 2012, ApJ, 761, 71

APPENDIX A: HALO CENTERING AND TRACKING

In this Appendix, we discuss how we computed the centre of the cosmological haloes from the *N*-body parti-

cles and tracked them between different snapshots of our simulations.

Our re-simulated haloes undergo very rapid mass growth and experience multiple major mergers over a short time-scale. This is problematic when attempting to define halo centres, and more so when linking haloes to their progenitors across simulation outputs. After some experimentation, we found that algorithms commonly used in the analysis of CDM simulations failed to yield satisfactory results under these extreme conditions. For instance, during a major merger a shrinking sphere algorithm would sometimes converge to the region between the two largest density peaks, and the position of the most bound particle was sensitive to how mass was divided between the different substructures, resulting in spurious temporal fluctuations in the recovered central structure.

To circumvent these issues, we define halo centres using a modified version of the shrinking sphere algorithm of Power et al. (2003). Our method uses an initial guess for the location of the halo centre and identifies all particles with a large radius r_i centred on that point. We then smooth the density field of these particles using a Gaussian kernel of size $0.1 \times r_i$, and identify its highest density maximum. The location of this peak is used as the new centre, and the radius of the sphere decreased by 20 per cent. This procedure is repeated until fewer than 1000 particles are found within r_i, at which point we adopt a traditional shrinking sphere algorithm. Using this centre, we then compute the virial mass, M_{vir}, and radius, R_{vir}, of the halo.

After computing halo centres in this way for a given simulation output, we then identify the most likely descendant of each in the subsequent snapshot. This is defined as the nearest halo in a hyperspace of position, virial mass, M_{vir}, and peak circular velocity, V_{max}. More specifically, the distance between a halo i at time t_i and a possible descendant halo j in a snapshot at time t_j is defined as

$$d_{ij}^2 = |x(t_j)^i - x^j|^{2/3} + \log(M_{vir}^i/M_{vir}^j)^{2/3} + \log(v_{max}^i/v_{max}^j)^{2/3},$$
(A1)

where $x(t_j)^i = x(t_i)^i + (t_i - t_j)v^i(t_i)H(t_i)$ is the predicted position of the halo i at time t_j. We found that this method performed more robustly than simply tracking a fraction of the most bound particles between simulation outputs, and gave consistent results during quiescent phases of halo growth.

APPENDIX B: ISOLATED HALO PARTICLE SAMPLING

In this Appendix, we discuss how we set up the haloes for our isolated non-cosmological merger simulations through which we study the evolution of halo density profiles during and after a sequence of major mergers.

B1 Setting up halo profiles by distribution function sampling

As discussed in Section 3.1.1, we consider spherically symmetric, isotropic DM halo models with truncated power-law density profiles:

$$\rho(r) = \rho_s \left(\frac{r}{r_s}\right)^{-\gamma} \text{erfc}[\kappa(r/r_s - 1)].$$
(B1)

For any spherically symmetric mass distribution, the gravitational potential is given by (Binney & Tremaine 2008, equation 2.28)

$$\Phi(r) = -\frac{GM(r)}{r} - 4\pi G \int_r^\infty dr' r' \rho(r'),$$
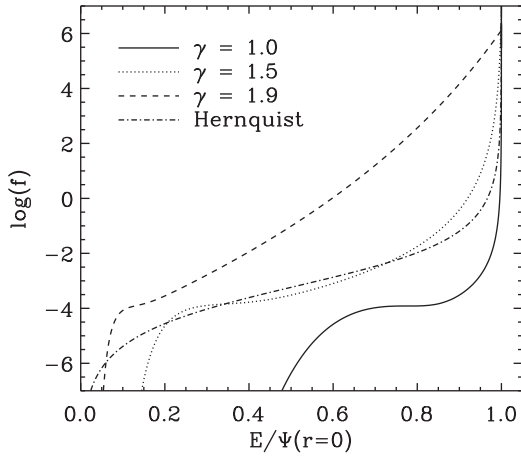(B2)

Figure B1. Distribution functions for our halo models (equation B1). Curves show results for three power-law indices, $\gamma = 1.0$ (solid line), $\gamma = 1.5$, (dotted line) $\gamma = 1.9$ (dashed line). The dot–dashed line shows the distribution function for a Hernquist profile.

where $M(r)$ is the total mass enclosed within a radius r, and G is Newton's gravitational constant.

The only ergodic distribution function that can lead to a spherically symmetric system is given by Eddington's formula (Binney & Tremaine 2008):

$$f(E) = \frac{1}{\sqrt{8}\pi^2} \left[\int_0^E \frac{d^2\rho}{d\Psi^2} \frac{d\Psi}{\sqrt{E-\Psi}} + \frac{1}{\sqrt{E}} \left(\frac{d\rho}{d\Psi} \right)_{\Psi=0} \right], \quad (B3)$$

where $E \equiv -\Phi(r) - \frac{1}{2}v^2$ is the relative energy, v is the velocity and $\Psi \equiv -\Phi$ is the relative gravitational potential. Note that since $\rho \to 0$ when $\Psi \to 0$, the second term in the above expression vanishes and equation (B3) can be rewritten as a function of only derivatives with respect to the radius:

$$f(E) = \frac{1}{\sqrt{8}\pi^2} \int_\infty^{r'(E)} \frac{dr}{\sqrt{E-\psi}} \quad (B4)$$

$$\times \left[\left(\frac{d\Psi}{dr} \right)^{-1} \frac{d^2\rho}{dr^2} - \frac{d\rho}{dr} \left(\frac{d\Psi}{dr} \right)^{-2} \frac{d^2\Psi}{dr^2} \right], \quad (B5)$$

where

$$\frac{d\Psi}{dr} = G \frac{M(r)}{r^2} \quad (B6)$$

$$\frac{d^2\Psi}{dr^2} = -2 G \frac{M(r)}{r^3} + 4\pi G \rho(r). \quad (B7)$$

The latter is more robust for numerical integration purposes. To solve for the distribution function, we first compute and tabulate $M(r)$, $\Psi(r)$, $d\rho/dr(r)$ and $d^2\rho/dr^2(r)$ using 2000 logarithmically spaced bins between $10^{-5} r_s$ and $10^3 r_s$. We perform the final integration using a Quadpack algorithm and interpolate the tabulated values when required. We note that an analytic solution for $f(E)$ is known for the case of a Hernquist density profile (Hernquist 1990). We use this to test our numerical implementation, finding agreement to better than 2 per cent over the whole range of allowed energies. We show the distribution functions for the density profiles considered in this paper in Fig. B1.

To create a stable initial configuration of particles, we first sample a radius r_i from the desired density distribution using an inverse
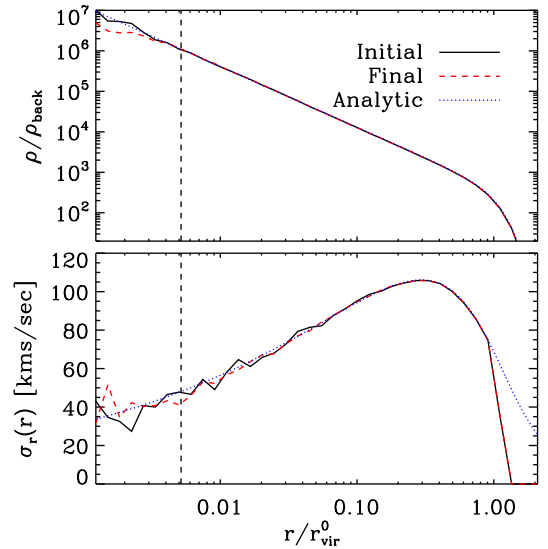

Figure B2. Comparison between the initial (solid black lines) and final states (dashed red lines) of an isolated DM halo model simulated with 10^6 particles for 10 Gyr. The top panel shows the measured density profiles together with the analytic expression of equation (B1); the bottom panel shows the radial velocity dispersion profile together with the solution of the Jeans equation for a spherically symmetric and isotropic system (blue dashed lines). The vertical dashed lines highlight $2.8 \times \epsilon$, the Plummer equivalent gravitational softening length used for our runs.

transform sampling. We then sample a velocity magnitude v_i from the distribution $f(v)dv = \sqrt{2(\Psi(r_i) - f(E))}vdv$ using a Neumann rejection method. The position and velocity of each particle are then assigned random orientations in order to ensure the system's isotropy.

B2 Testing stability

In order to assess the stability and accuracy of our models, we created a single halo with a ($\gamma = 1.5$) power-law density distribution and evolved it in isolation. In Fig. B2, we show the initial and final density and velocity dispersion profiles. For comparison, blue dotted lines show the analytic density profile and the velocity dispersion profile computed using the Jeans equation for a spherical system with an isotropic velocity distribution. We note that the simulated halo agrees extremely well with the analytic results, showing small differences only in the central regions where particle noise is not negligible. In addition, the system is dynamically extremely stable: the final state agrees remarkably well with the analytic results as well as with the initial configuration, with very little departure over the entire range plotted. Small differences are most clearly seen in the very inner parts of the halo ($r < 0.005r_{vir}$), where the relaxation times are short and two-body scattering becomes important. However, this occurs on scales smaller than the formal resolution scale of our simulations. Therefore, these results validate our implementation as well as the integration and force calculation accuracy of our simulations.

This paper has been typeset from a TeX/LaTeX file prepared by the author.